International Journal of Rock Mechanics & Mining Sciences 174 (2024) 105642

Contents lists available at ScienceDirect

International Journal of Rock Mechanics and Mining Sciences

journal homepage: www.elsevier.com/locate/ijrmms

Mechanisms of stress- and fluid-pressure-driven fault reactivation in Gonghe granite: Implications for injection-induced earthquakes

Chongyuan Zhang [a,b,c,*], Dongjue Fan [a,d], Derek Elsworth [e], Manchao He [b], Xingguang Zhao [f], Chun Zhu [g], Hao Zhang [a,c]

[a] Institute of Geomechanics, Chinese Academy of Geological Sciences, Beijing, 100081, China
[b] School of Mechanics and Civil Engineering, China University of Mining and Technology, Beijing 100083, China
[c] Technology Innovation Center for In-situ Stress, Ministry of Natural Resources, Beijing 100081, China
[d] School of Civil and Resource Engineering, University of Science and Technology Beijing, Beijing, 100081, China
[e] Energy and Mineral Engineering, EMS Energy Institute and G3 Center, Pennsylvania State University, University Park, 16802, USA
[f] CNNC Key Laboratory on Geological Disposal of High-level Radioactive Waste, Beijing Research Institute of Uranium Geology, Beijing 100029, China
[g] School of Earth Sciences and Engineering, Hohai University, Nanjing, 210098, China

ARTICLE INFO

Keywords:
Enhanced geothermal systems
Injection-induced earthquakes
Fault reactivation
Gonghe granite
Rock mechanics

ABSTRACT

We explore the impacts of stress- and fluid-pressure-driven frictional slip on variably roughened faults in Gonghe granite (Qinghai Province, China). Slip is on an inclined fault under simple triaxial stresses with concurrent fluid throughflow allowing fault permeability to be measured both pre- and post-reactivation. Under stress-drive, smooth faults are first slip-weakening and transition to slip-strengthening with rough faults slip-strengthening, alone. A friction criterion accommodating a change in friction coefficient and fault angle is able to fit the data of stable-slip and stick-slip. Under fluid-pressure-drive, excess pore pressures must be significantly larger than average pore pressures suggested by the stress-drive-derived failure criterion. This overpressure is conditioned by the heterogeneity of the pore pressure distribution in radial flow on the fault and is related to the change in permeability. Fault roughness impacts both the coefficient of friction and the permeability and therefore exerts important controls in fluid-injection-induced earthquakes. The results potentially improve our ability to assess and mitigate the risk of injection-induced earthquakes in Enhanced geothermal systems.

1. Introduction

Fluid injection is a preferred method for the stimulation of Enhanced Geothermal Systems (EGS) to elevate permeability from micro-to milli-Darcy levels. Fluid injection-induced reductions in effective stress are capable of reactivating fractures. The key is to generate permeability through shear reactivation but avoid creating runaway slip that can trigger large seismic events.[1] Since 2019, China has initiated its first EGS development project in the Gonghe basin on the northeastern extent of the Tibetan plateau.[2] The northeastern part of the Qinghai–Tibet Plateau is a tectonically active area with a high risk of strong earthquakes.[3,4] In 1990, a Mw 6.4 earthquake occurred ~30 km from the Gonghe EGS site.[5] The Gonghe EGS is in a still higher stress environment with a further elevated risk of injection-induced seismicity. Controls on fluid injection induced seismicity on variable roughness faults under non-stationary and strongly heterogeneous distributions of pore fluid pressures remain unclear. To address this issue, we complete experiments and analytical characterizations on laboratory faults under various normal stress and fluid pressure stress paths.

Characterizations of fault friction based on constant friction[6] are unable to replicate stick-slip phenomena observed during earthquakes. Rate- or velocity-weakening response is a necessary requirement[7,8] to replicate this behavior. Slip weakening may be defined over a slip weakening distance[9] and as a function of state.[10] These relations usually define the evolution of second-order frictional effects under prescribed velocity conditions and under constant effective stress - but stress paths are rarely simple and fluid injection reactivations can be strongly varying in both space and time.

Injection-induced earthquakes are impacted by the minimum principal stress,[11] the total volume of injected fluid[12] or related to Gutenberg-Richard statistics.[13,14] These models assume that pore pressure is uniformly distributed during fluid injection, but laboratory tests

* Corresponding author. Institute of Geomechanics, Chinese Academy of Geological Sciences, Beijing, 100081, China.
E-mail addresses: zhchongyuan@126.com, zhangchy@cags.ac.cn (C. Zhang).

https://doi.org/10.1016/j.ijrmms.2024.105642
Received 23 July 2023; Received in revised form 9 October 2023; Accepted 4 January 2024

and field studies show that the fluid pressure required to activate a fault is often higher than that predicted using the Mohr–Coulomb failure criterion. An uneven diffusion of fault overpressure substantially affects the stress field and fault stability. The overpressure distribution,[15,16] together with the heterogeneous diffusion of pore pressure[17–19] impact fault instability driven by injection. During the injection, the distribution of pore pressure in a fault is influenced by various factors such as fault roughness, in-situ stress state, mineral composition, and injection conditions.[20] These factors are implicit in defining the heterogeneous permeability of faults and thereby the uneven distribution of pore pressure.

At present, several experimental methods have been developed to simulate the frictional slip on rock faults. According to the characteristics of loading, they can be divided into single direct shear, double direct shear, rotary shear, and triaxial shear testing configurations. Single direct shearing is conducted by fixing the lower fault and applying normal and shear loads to the upper block.[21,22] This method has simple stress boundary conditions, but the load distribution on the fault surface is not uniform due to its loading characteristics. Double direct shearing uses three blocks with two parallel fault interfaces to apply a near uniform and moment-free shear stress to two fault surfaces.[23] This enables a more uniform distribution of shear load on the fault surface. Under rotary shear,[24,25] the shear stress is applied by fixing the upper/lower part of a toroidal rock sample and rotating the lower/upper part around a central axis under applied normal stress. This method can represent both high shear rates and large shear displacements. However, rotary shear has difficulty in applying large excess pore pressures to the fault. Triaxial shear tests allow inclined faults traversing a cylindrical sample to be reactivated.[26,27] Cylindrical rock samples containing 45°–60° prefabricated fractures are used to concurrently apply normal and shear stress to the laboratory fault *via* confining pressure and axial stress. Triaxial shear tests allow control of the ratio of normal to shear stress through the selection of fault angle as a complex stress together with the ready application of temperature and pore pressures.

To address the mechanism of stress- and fluid-pressure-driven instability of various roughness faults we complete experiments and analytical characterizations on laboratory faults under various total stress and fluid pressure stress paths. The mechanical (stress and displacement) and transport characteristics (pore pressure and permeability) of faults with different surface roughness were characterized to constrain frictional slip under both total stress- and fluid-pressure-driven stress paths. Finally, we discuss the effect of fault roughness and permeability on injection-induced earthquakes to improve our ability to assess and mitigate the risk of anthropogenic earthquakes in EGS.

2. Materials and methods

The granites used in this study are surface outcrop derived samples of granites from the Gonghe basin, Qinghai Province, China. These granites are 37 % quartz, 33 % microplagioclase, 25 % mica, 3 % amphibole, and 2 % plagioclase[28] by volume. The resulting cylindrical samples are 50 mm in diameter and 100 mm in height and contain a diamond sawcut fault inclined at 45° and pierced by two 1.5-mm-diameter boreholes accessing pressurized fluids from the end platens. The boreholes were used to change pressures and therefore effective stresses and also to measure permeability before and after slip. The fault surfaces are roughened with sandpaper corresponding to particle sizes of 150 μm, 23 μm, and 1.3 μm, for different fault roughnesses. A Top Industrie high-temperature triaxial testing system was used to conduct the reactivation experiments. The maximum axial load of the system is 1500 kN with confining pressures and pore pressures in the range 0–60 MPa. Silicon oil is used as the confining fluid. The sample and test configuration are shown in Fig. 1.

A total of nine rock samples were produced from the same surface outcrop sample with the cylindrical samples divided into three groups according to the variable roughnesses of the fault surfaces. Sample information is shown in Table 1.

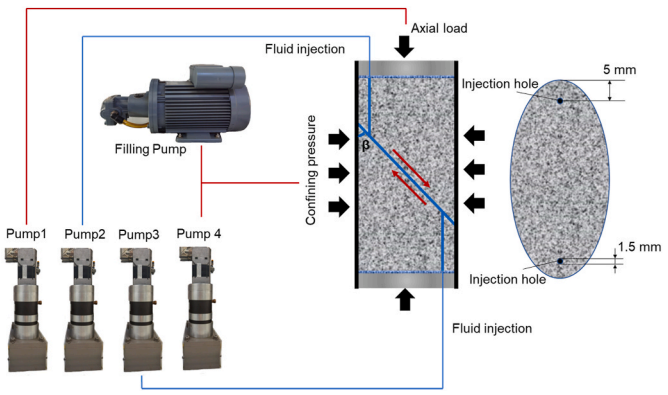

Fig. 1. Schematic of rock sample and testing configuration. Four pumps separately regulate the axial pressure, confining pressure and the pore pressure at both ends of the sample.

Each test consists of two separate stress paths: stress-driven frictional slip followed by fluid-pressure-driven frictional slip. Specific test procedures are described as follows.

Step 1: **Initial state.** The sample was vacuum saturated with deionized water and then sealed by polyurethane sleeves before hydrostatic loading ($\sigma_1 = \sigma_2 = \sigma_3$). Previous research has shown that the friction coefficients of fault in rock decrease as a result of pore water presence.[29] In order to ensure that the fault is always saturated during the test, a pore pressure of 1 MPa was then applied to saturate the fault before being reduced to 0.5 MPa. Fault permeability was measured for steady state flow[30] with an upstream (1.5 MPa) to downstream (0.5 MPa) pore pressure differential of 1 MPa.

Step 2: **Stress-driven fault activation**. We selected constant axial stress as a load target in order to ensure that faults with different roughness are at the same stress level before injection. Axial stress targets were larger than the reactivation stress of the fault and increased with the confining pressure as shown in Table 1. Axial stress was applied at 0.01 MPa/s according to the experimental schedule of Table 1 and the confining pressure remained constant. As shown in Fig. 2, the fault experiences a high normal stress while the shear stress is zero before loading. With the loading process advances, both normal and shear stresses on the fault increase concurrently. Consequently, the ratio of fault shear stress to normal stress gradually diminishes. When the shear stress exceeds the maximum frictional strength the fault, the fault slips and the static frictional strength was recorded to calculate the coefficient of friction. Subsequently, the fault went through the initial strain hardening stage until the axial stress retained constant. Fault permeability was measured using the method of Step 1.

Table 1
Rock sample characteristics and experiment matrix.

Sample Number	Size of sandpaper (μm)	Confining pressure (MPa)	Axial stress (MPa)	Load rate (MPa/s)	Injection rate (mL/s)
1–1	150	10	34	0.01	0.05
1–2	150	20	68	0.01	0.05
1–3	150	40	136	0.01	0.05
2–1	23	10	34	0.01	0.05
2–2	23	20	68	0.01	0.05
2–3	23	40	136	0.01	0.05
3–1	1.3	10	34	0.01	0.05
3–2	1.3	20	68	0.01	0.05
3–3	1.3	40	136	0.01	0.05

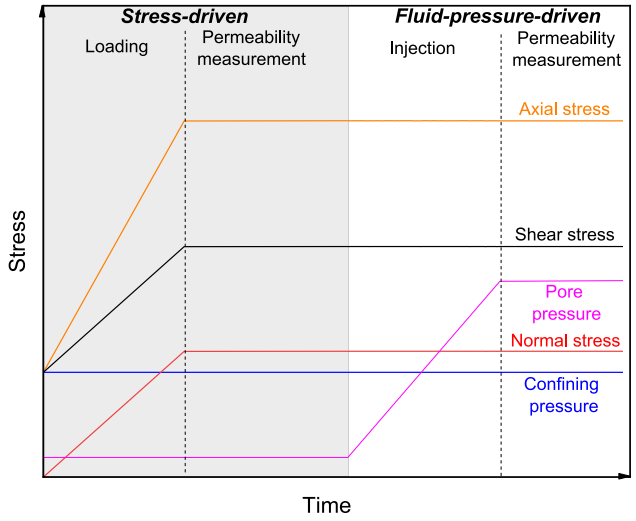

Fig. 2. Schematic of test procedures. Each test consists of two separate stress paths: stress-driven frictional slip followed by fluid-pressure-driven frictional slip. Under stress-driven, the shear stress and normal stress increase synchronously; Under injection-drivrn, the normal stress and shear stress in the fault remain constant, and the pore pressure increases gradually.

Step 3: **Fluid-pressure-driven fault reactivation.** Deionized water was injected into both boreholes simultaneously at a rate of 0.05 cm^3/min after the fault reached steady state. The increase in pore pressure leads to a decrease in effective normal stress and the reactivation of fault slip – that reactivation pore pressure is recorded. The pore pressure continues to increase to 50 % of the confining pressure after reactivation. Then, the outlet pore pressure was retained constant and the inlet pore pressure increased by 1 MPa with the fault permeability measured as above.

The axial force applied to the sample is usually measured using a load cell located outside the pressure vessel. In this case, however, part of the measured force is resisted by the friction between the moving piston and the confining sealing assembly.[31] Therefore, a load cell was located inside the confining pressure vessel to measure true axial force applied to the sample. The axial force was also corrected by considering and calibrating out jacket restraint during the tests.[32]

The axial displacement (Δl) can be obtained from a linear variable displacement transducer (LVDT) installed on the sample. The fault slip displacement (u) can therefore be estimated as,

$$u = \left(\Delta l - \frac{\sigma_1 \cdot l}{E}\right) \cdot \frac{1}{cos\,\beta} \tag{1}$$

where β is the dip angle of the fault surface (in our case, $\beta = 45°$), E is the Young's modulus of the granite, σ_1 is axial stress and l is the length of the cylindrical sample. In this study, axial stress σ_1 is computed by dividing the uncorrected stress by the factor A/A_0,

$$\frac{A}{A_0} = (\theta - sin\,\theta) \Big/ \pi \tag{2}$$

$$\theta = \pi - 2\,sin^{-1}[(u/dr)tan\,\beta] \tag{3}$$

where θ is the angle subtended by the points of intersection of two overlapping circles. At the centers of the circles, A_0 and A are the original and corrected cross-sectional areas of the sample. In this study, the maximum fault shear displacement does not exceed 2 mm, and the area correction results in a stress adjustment of 3.59 % at 2 mm.

The normal stress and shear stress on the fault surface in the center of the sample were calculated from the axial stress σ_1 and confining pressure σ_3 as:

$$\tau = \frac{1}{2}(\sigma_1 - \sigma_3)sin\,2\,\beta = (\sigma_1 - \sigma_3)sin\,\beta\,cos\,\beta \tag{4}$$

$$\sigma_n = \frac{1}{2}[(\sigma_1 + \sigma_3) - (\sigma_1 + \sigma_3)cos\,2\,\beta] = \sigma_3 + (\sigma_1 - \sigma_3)sin^2\,\beta \tag{5}$$

For the elliptical fault with two boreholes, the transmissivity was calculated based on the electrical analogy.[33] In order to simplify the evaluation of the fracture permeability, we assumed a rectangular flow region with an area equal to that of the ellipse.[27] The aperture used to calculate permeability was determined from the cubic law.

$$e_h = \left(-\frac{12\nu LQ}{gwJ}\right)^{1/3} \tag{6}$$

where Q is the volumetric flow rate within the fracture, w is the width of the cross-sectional area of flow between parallel plates, L is the distance between the two boreholes on fracture surface, ν is the kinematic viscosity of the fluid, g is the gravitational acceleration and J is the hydraulic gradient of unity. By measuring the flow rate of the fault, the equivalent hydraulic aperture e_h can be determined. Combined with Darcy's law, the permeability k of the fracture can be obtained from

$$k = \frac{{e_h}^2}{12} \tag{7}$$

All data are acquired in real-time at a sampling rate of 10 Hz with fault roughness measured by a 3D laser scanner both pre- and post-test to define evolving damage characteristics of the fault surface during the reactivation.

3. Experimental result

3.1. Fault slip characteristics

The shear stress on the fault is normally obtained by a displacement-driven shear test which is carried out at an axial displacement rate.[34] While displacement-driven experiments can provide valuable insights into fault slip behavior and friction coefficient changes under controlled displacement conditions, stress-driven experiments better simulate real-world geological conditions and provide accurate stress-slip relationships. In order to obtain the intact slip characteristics of fault slip and ensure that faults with different roughness are subjected to the same stress level during permeability measurements, a constant loading rate is employed instead of a constant displacement rate. Fig. 3a–c shows the stress/pressure/displacement versus time behavior under stress- and then fluid-pressure-driven reactivation (using a representative example at a confining pressure of 20 MPa). In stress-driven fault activation, the stable stage in which shear displacement does not increase on a fault can be observed clearly. As the axial stress continues to increase, the fault slips at a constant shear rate after an acceleration. At this time, the fault enters the steady-state initial condition after the initial strain hardening period.

Subsequently, the faults with varied roughness showed different reactivation characteristics under stress-driven conditions. For the roughest fault (roughened at 150 μm; Fig. 3a), the fault reactivated with stable-slip that stopped when the axial loading was stopped. For the medium-roughness fault (roughened as 23 μm; Fig. 3b) a small stress drop occurred after reactivation before stable slip resumes. Finally, the smoothest fault (a particle size of 1.3 μm; Fig. 3c) reactivates in stick-slip with a large stress drop and shear displacement and accompanied by an audible noise. Multiple stick-slips followed until the axial stress remained stable after the fault slip stopped. In addition, the peak stress in rock sample 3-3 was limited by repeated stick-slip, preventing it from reaching the target axial stress value. Therefore, a liquid injection-induced slip test was carried out while keeping the axial stress at 100 MPa.

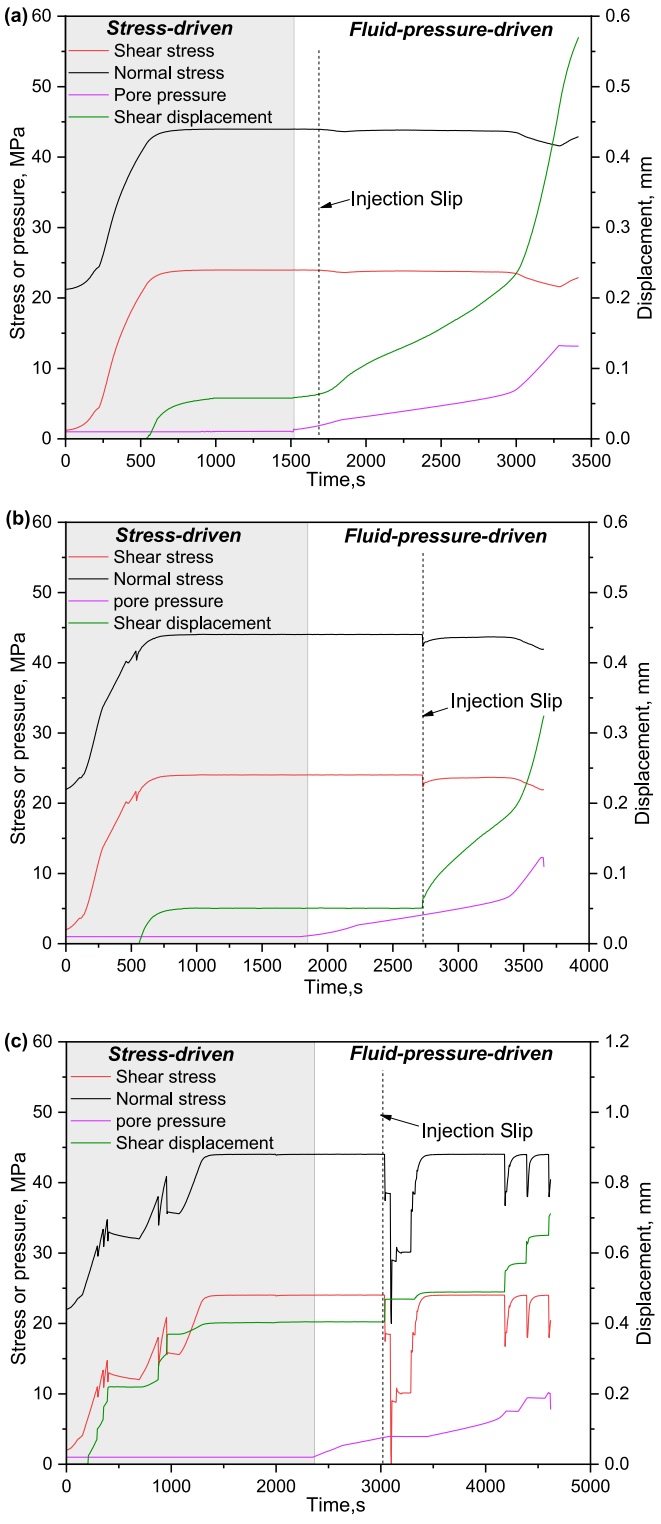

Fig. 3. Stress, displacement, and pore pressure histories for the stress- and fluid-pressure-driven reactivation experiments: (a) Rough sample 1–2 (size of sandpaper:150 mm, confining pressure:20 MPa), (b) Intermediate roughness sample 2-2 (size of sandpaper:23 mm, confining pressure:20 MPa), and (c) smooth sample 3–2 (size of sandpaper:1.3 mm, confining pressure:20 MPa). The first half of the time history is under stress-driven conditions and the second half under fluid-pressure-driven conditions.

Following the stress-driven reactivations, the samples were again reactivated by fluid pressures – and again reactivated in contrasting styles according to fault roughness. For smooth rock samples, a continuous stick-slip phenomenon occurred during the fluid injection.

When the fluid pressure is uniform on the fracture surface, the effective normal stress σ_{en} on the fault surface is equal to the difference between the normal stress σ_n and pore pressure P_W as:

$$\sigma_{en} = \sigma_n - P_w \tag{8}$$

Fig. 4 shows the Mohr-Coulomb failure envelopes for the faults during stress-driven and fluid-pressure-driven reactivations. We construct the failure envelopes for the faults by fitting the shear strengths obtained from the stress-driven frictional slip experiment, and derive the maximum static friction coefficients for the faults polished by 150 μm, 23 μm, and 1.3 μm grit sandpapers as 0.53, 0.50, and 0.24, respectively. The shear stress on the faults gradually increased and then remained constant after axial loading was stopped. Fluid was then injected into the fault at a constant injection rate and the effective normal stress reduced. Although the fault was already critically stressed, the fault does not reactivate until its stress state reaches a new envelope (blue dashed line). The pore pressure measured from the injection boreholes is thus larger than that predicted by the failure criterion. This is similar to the overpressure phenomenon found in other experiments and field studies[35–37] representing a higher reactivation friction coefficient for fluid injection versus a change in normal stress.

3.2. Fault damage characteristics

A three-dimensional (3-D) laser scanning system, with a 10 μm resolution laser beam, was used to measure the topography of the fault surfaces. Typical profiles of the fault surface both before and then after slip are shown in Fig. 5. The main signature of the reactivation deformation is striations as damage along the slip direction. After the test, the fault surface was observed by microscope and few wear products were present on the fault surface. This is consistent with the phenomena observed in previous studies.[27,38,39] In this case, the smooth saw-cut fault does not develop a significant gouge layer during the reactivation. The fault surface only produces a small amount of damage as concave striations.

The volume of the concave striations on the fault surface caused by the damage was used to characterize the damage on the fault surface during slip.[40] This is equivalent to the height and the area of the concave striations. The damage volume of each fault (shown in Table 2) is minute as compared to rough natural faults.[34] The thickness of the fault gouge can be estimated by dividing the volume of damage by the area of the fault. In this study, the calculated thickness of the fault gouge was found to be approximately 0.24 μm.This indicates that the surface damage of the sawcut fault used in this work is much less than that of natural faults.

Fault slip characteristics are also affected by the uneven distribution of fault surface roughness.[41] The roughness of the fault surface is uniformly distributed before the test. However, it is possible to reorganize the distribution of roughness during slip due to the uneven distribution of damage. We use the standard deviation of fault damage depth to characterize the heterogeneity of fault damage (shown in Table 2). The standard deviation of each rock sample is small, at 0.04–0.07 μm, indicating that the damage distribution on the fault surface is relatively uniform.

3.3. Fault permeability characteristics

Fault slip reactivation may substantially affect the aperture of faults and hence permeability. Permeability may change in sense depending on the mineral composition, stress conditions, surface roughness, and shear displacement of the rock.[20] Fault permeability also influences the rate of pore pressure diffusion within the fault. In this study, the permeability of faults has been measured from the initial state, after

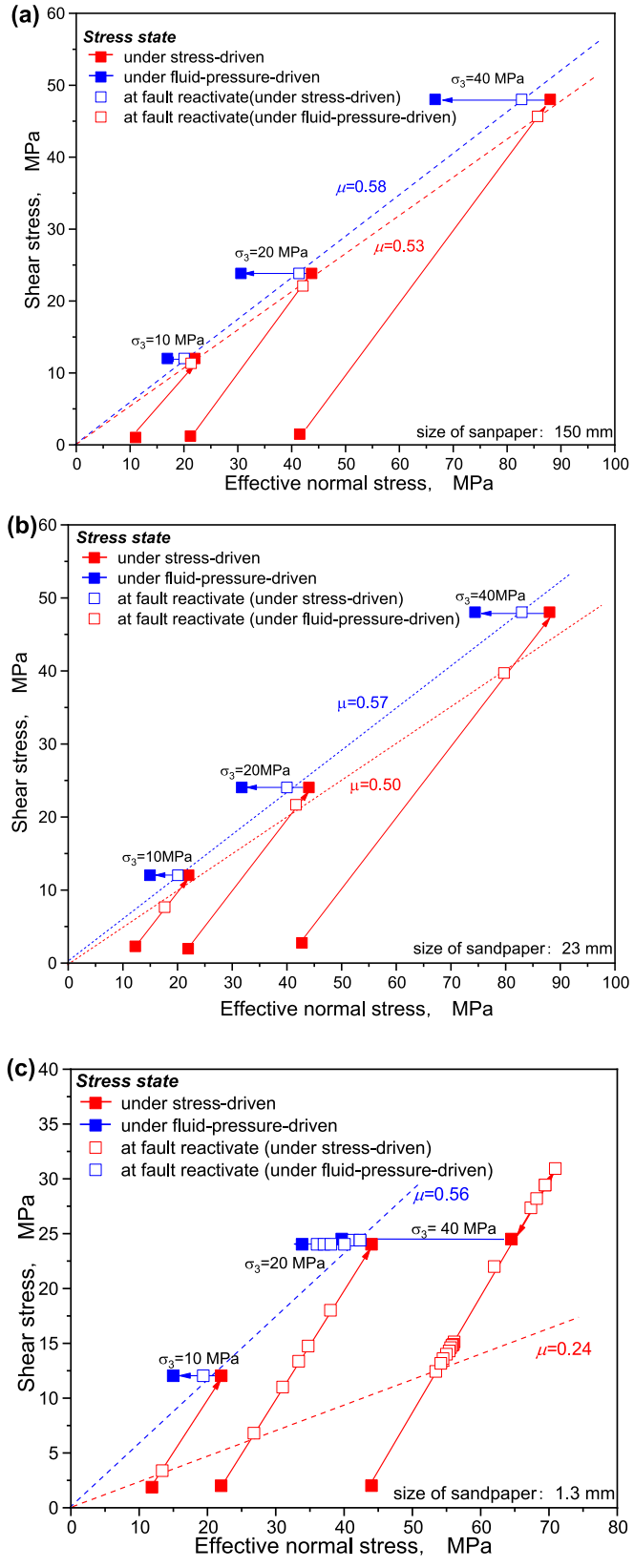

Fig. 4. Mohr-Coulomb failure envelopes for laboratory faults reactivated by stress- and fluid-pressure-driven: (a) Samples polished to 150 μm roughness under confining pressures of 10 MPa, 20 MPa, and 40 MPa; (b) Samples polished to 23 μm roughness under confining pressures of 10 MPa, 20 MPa, and 40 MPa; (c) Samples polished to 1.3 μm roughness under confining pressures of 10 MPa, 20 MPa, and 40 MPa.

both stress-driven fault reactivation and then after fluid-pressure-driven fault reactivation, respectively. The initial values of permeability for each rock sample are shown in Fig. 6a.

To obtain the evolution of permeability under fault reactivation, the fault permeability and shear displacements were normalized with respect to the initial permeability and maximum shear displacement following reactivation. Fig. 6b–d shows the normalized permeability and the normalized shear displacement of the various faults after stress-driven reactivation. The fault permeability decreases with an increase in shear displacement as a result of generation of wear products, development of a sliding surface and compaction of fault and resulting gouge under stress-drive.[20,42–44] For a natural rough fault, the evolution of asperity geometry and distribution modifies the fracture aperture and the flow velocity and subsequently enhancement the fault permeability.[45] However, the smooth fault surfaces in this study cannot drive significant fracture dilation. The fault damage characteristics noted in Section 3.2, representing shallow striations of damage on the fault surface, do not promote significant shear dilatancy.

The fault permeability increased under fluid-pressure-driven. This is opposite to the trend in permeability change under stress-driven condition. Generated wear products of low surface roughness fractures would seal the fluid conduits of fracture aperture, countering the effect of fracture dilation. However, it is important to highlight that the surface damage observed on the sawcut fault is significantly lower in comparison to the typical damage observed on natural faults, as discussed in Section 3.2. In this condition, the major contributor to permeability enhancement is the normal dilation resulting from the increase of pore pressure in fault.[45] This results in a significant increase in the permeability of smooth faults, up to 36 times higher than the initial permeability (Fig. 6d). The permeability enhancement during fracture shearing is highly dependent on fault roughness and stress state.[45]

4. Discussion

4.1. Mechanism of fault activation under stress-drive conditions

The mechanism of fault slip under stress-drive conditions may be explored by investigating the evolution of mechanical properties (shear and normal stress, shear displacement, friction coefficient and shear velocity). It is suggested that data sampled at less than 10 Hz may underestimate the values of the dynamic slip events.[46,47] Therefore, we will not discuss the rate of fault slip. In Fig. 7, The friction coefficient is obtained by the ratio of shear stress to normal stress. Three stages of fault reactivation can be defined under stress-drive conditions according to the evolution of shear displacement.

(1) **Stability stage:** When axial stress is applied during loading, the shear stress on the fault surfaces is still insufficient to overcome the frictional resistance, and the fault remains in a stable state.
(2) **Initial slip stage:** Shear stress exceeds the peak static friction and shear displacement begins to increase. The shear displacement increases linearly with the shear stress after an acceleration. At this time, the fault enters a steady-state initial condition after the initial run-in period.
(3) **Continuous slip stage:** As the axial stress continues to increase, high roughness faults (Fig. 7a, using a representative example of sample 1–3) remain in stable-slip and the friction coefficient increases with slip. For a smooth fault (Fig. 7b), the fault reactivates in stick-slip with a stress drop and shear displacement jump. The friction coefficient changes from the maximum static friction coefficient to the dynamic friction coefficient during this period. With an increase in the normal stress and shear stress, the friction coefficient gradually increases until the loading stops or the next stick-slip occurs.

According to the three stages of fault slip, the change in friction

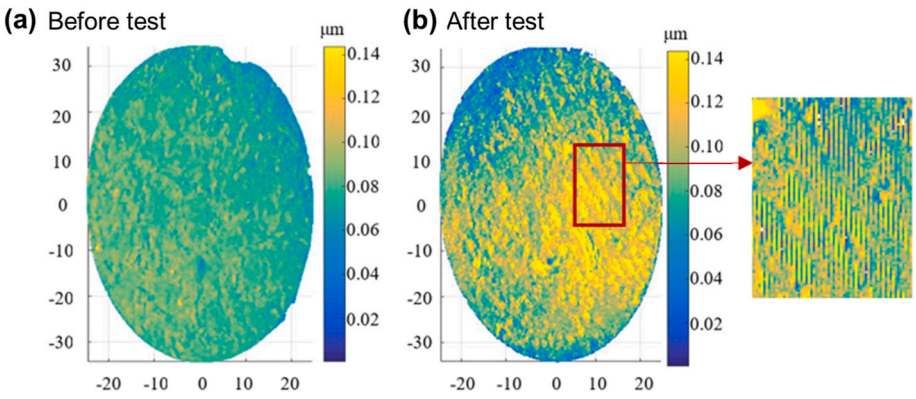

Fig. 5. Damage on fault surfaces during reactivation. Typical scanning results of fault before (a) and after (b) test.

Table 2
The standard deviation of damage on fractured rock samples.

Sample number	Confining pressure (MPa)	Damage standard deviation (μm)			Volume of damage (mm^3)
		A	B	Average	
1–1	10	0.0482	0.0441	0.04615	2.711
1–2	20	0.0408	0.0474	0.0441	2.729
1–3	40	0.0497	0.0561	0.0529	2.769
2–1	10	0.0469	0.0429	0.0449	2.748
2–2	20	0.0417	0.0409	0.0413	2.762
2–3	40	0.0444	0.0616	0.053	2.788
3–1	10	0.0536	0.0511	0.05235	2.641
3–2	20	0.0495	0.0487	0.0491	2.665
3–3	40	0.049	0.0672	0.0581	2.695

coefficient is related to the fault stress state, slip distance, and slip characteristics (stable-slip or stick-slip) during continuous stress loading. At present, the four most widely used models to describe fault slip are rate weakening,[48] rate- and state-dependent models with either an aging law[49] or slip law,[50] and slip weakening friction.[51] Among them, the first three require rate data during slip. These data are difficult to recover for practical engineering applications. According to the friction law related to slip weakening, the change in friction coefficient with slip shows a linear or nonlinear relationship. The friction relationship for slip weakening under linear conditions can be described as[51]:

$$\tau = \begin{cases} \left[\mu_s - (\mu_s - \mu_f)\dfrac{u}{d_0}\right]\sigma_n, d < d_0 \\ \mu_f \sigma_n, d > d_0 \end{cases} \quad (9)$$

where μ_f and μ_s are the maximum dynamic friction coefficient and static friction coefficient, respectively; d is the relative slip displacement between upper and lower fault surfaces; σ_n is the normal stress on the fault surface; d_0 is the characteristic slip distance, representing the slip distance required for the static friction coefficient to decrease to the dynamic friction coefficient.

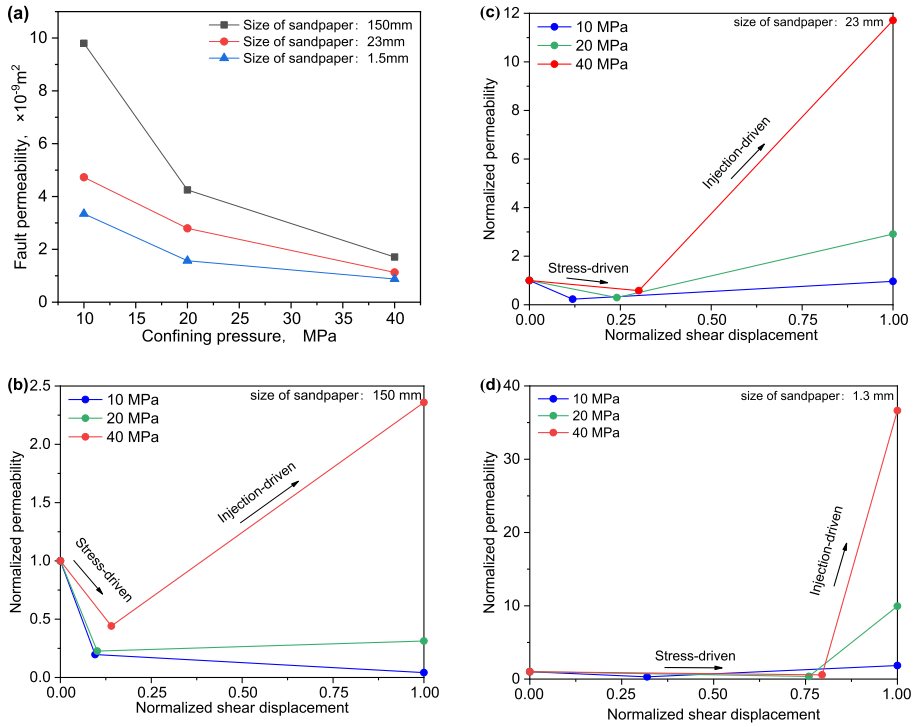

Fig. 6. Normalized fault permeability as a function of normalized shear displacement: (a) Measurement results of fracture permeability with different roughness before tests; (b) Samples polished to 150 μm roughness under confining pressures of 10 MPa, 20 MPa, and 40 MPa; (c) Samples polished to 23 μm roughness under confining pressures of 10 MPa, 20 MPa, and 40 MPa; (d) Samples polished to 1.3 μm roughness under confining pressures of 10 MPa, 20 MPa, and 40 MPa.

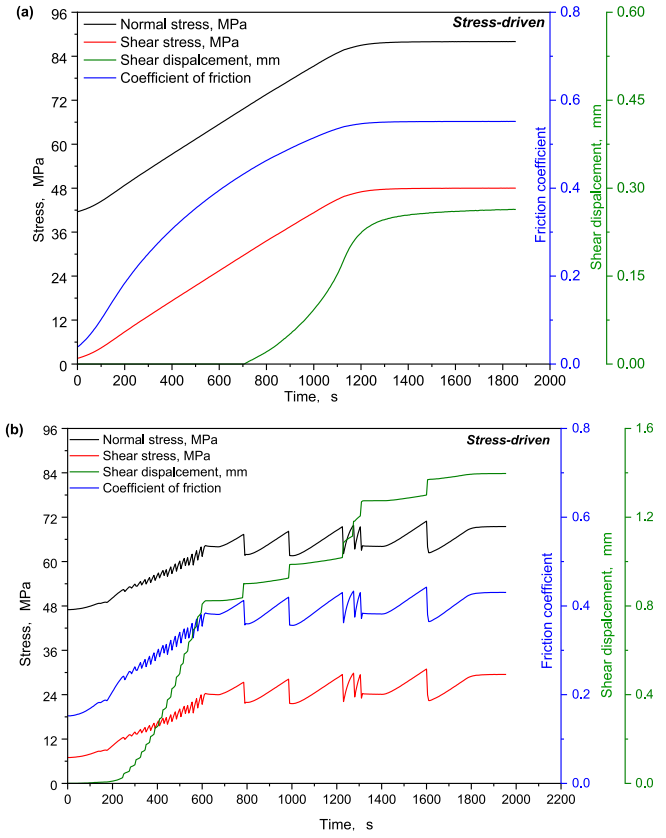

Fig. 7. Change in mechanical properties during stress-driven frictional slip: (a) Stable-slip; (b) Stick-slip.

Therefore, the analysis of friction slip mechanism of faults under stress-driven condition can be described as follows: As shown in Fig. 8a, the transition from the initially stable stage to slip can be explained by the Mohr-Coulomb failure criterion. Fault slip occurs when the shear stress on the fault exceeds its maximum static frictional resistance. Faults with a high roughness primarily exhibit stable slip behavior (Fig. 8b). As depicted in Fig. 8c, faults with low roughness exhibit rapid

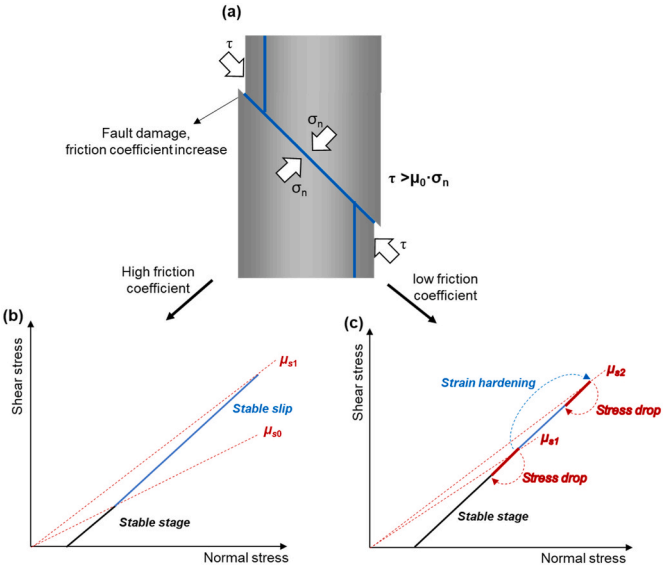

Fig. 8. Mechanisms of fault reactivation under stress-driven: (a) Schematic of fault instability; (b) Stable slip under stress-driven conditions; (c) Stick-slip under stress-driven conditions.

slip accompanied by a significant stress drop, leading to stress relaxation and subsequent transition into stable-slip state. Following stick-slip events, the frictional force on the fault plane increases due to fault plane deformation and the redistribution of frictional forces. Consequently, a higher stress is required to overcome the incremental frictional force during slip. Moreover, rocks on the fault plane undergo strain hardening during fault slip, resulting in a reduced ability to deform. As a result, a higher stress is needed to counteract the amplified frictional forces post-slip. Therefore, with multiple slip events, the friction coefficient of the fault gradually increases until the strain region on its surface stabilizes. At this stage, the shear strength of the fault remains relatively constant during continuous stick-slip, as shown in Fig. 7b.

In addition, when using Eq. (9) to calculate frictional slip, it is necessary to obtain the characteristic slip length d_i. In stick slip, the slip distance of the fracture is often related to the difference in the stress on the fracture surface from before until after slip.[52] The stress drop is calculated as:

$$\Delta\sigma = \sigma_0 - \sigma_1 \tag{10}$$

If the stress drop distribution of historical earthquakes is known, then the dynamic process of earthquake rupture may be illuminated. The characteristic slip length d_0 increases with the stress drop. Because of the non-uniform distribution of stress and strength near the fault, the relationship between slip distance and stress drop is generally complex. Two methods are primarily used to evaluate stress drop. The first is to apply a scaling relationship based on comparing the earthquake magnitude with its radiated energy or the estimated fault rupture area.[53] The second is to estimate the stress drop by finding the relevant parameters in the model through a source spectrum analysis based on an assumed source model. Where the source spectrum analysis is used, a disc fault model is generally assumed for small and medium-sized earthquakes. Here, a disk of radius R, is subject to a stress drop $\Delta\sigma$ as

$$\Delta\sigma = \frac{7}{16}\frac{M_0}{R^3} \tag{11}$$

where M_0 is the seismic moment. This moment may be evaluated from the shear modulus G of the fractured rock mass[54] as,

$$M_0 = GSd \tag{12}$$

where, S is the area of the fault, m^2. G can be considered as the combined rigidity of the test system and the fracture and can be determined based on the least squares method to achieve the minimum value of the sum of squared residuals[55]:

$$G = \frac{M_0 \sum_{i=1}^{n} d_i}{S \sum_{i=1}^{n} \left(d_i^2\right)} \tag{13}$$

Fig. 9 shows the relationship between slip distance and stress drop during the stick-slip cycle. The trends of stress drop and slip displacement remain the same under both stress- and injection-drive. Assuming that the piston of the machine remains constant during stick-slip, the stiffness K of the rock sample and loading system is related to the stress drop $\Delta\tau$ and the slip distance d_i during stick-slip[50]:

$$K = \Delta\tau / d_i \tag{14}$$

The combined rigidity is recovered from the least squares method and results in a best-fit value of 95.405 MPa/mm ($R^2 = 0.90$). The fitting results agree well with the stress drop and slip displacement measured directly in the tests, indicating that the derived rigidity is reasonable. By monitoring the magnitude of the stress drop on the fault surface, the characteristic slip value d_0 can be obtained, and the entire fault slip process followed.

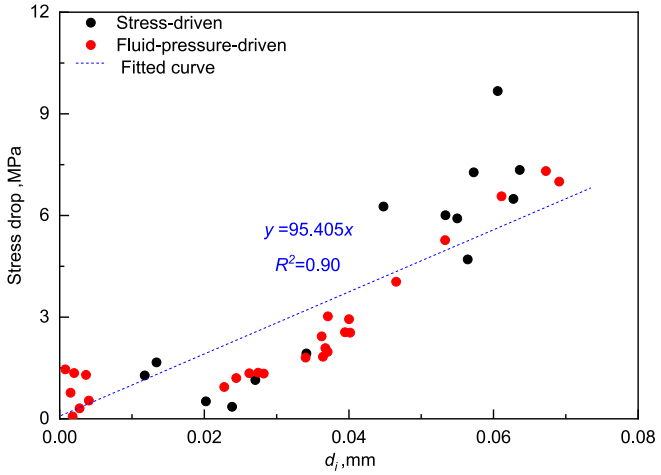

Fig. 9. Stress drop with slip distance. Black points are the experimental data under stress-driven; Red points are the experimental data under fluid-pressure-driven. The blue dotted line is obtained by jointly fitting the experimental data under stress-drive and fluid-pressure-driven. (For interpretation of the references to colour in this figure legend, the reader is referred to the Web version of this article.)

4.2. Mechanism of fault reactivation under fluid-pressure-driven condition

Fig. 10 shows typical slip distance versus friction coefficient results for stable slip and stick–slip processes. Frictional slip under fluid-pressure-drive can also be divided into three stages: a stable stage, an initial slip stage then a continuous slip stage, similar to the slip

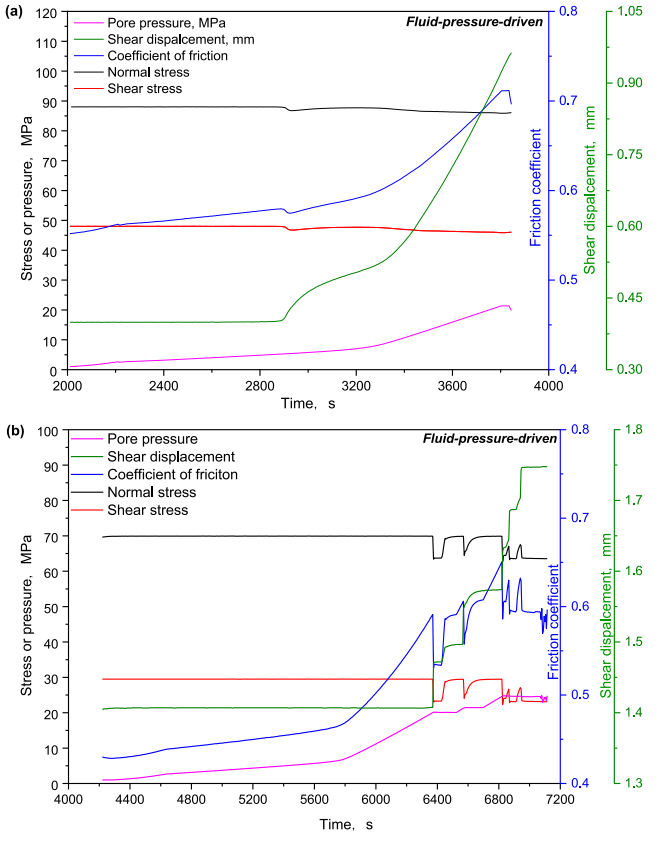

Fig. 10. Evolution of mechanical properties under fluid-pressure-driven: (a) Smooth fault; (b) Rough fault.

characteristics under stress-drive. In the stable stage, despite the increase in pore pressure, the fault does not slip. In the initial slip stage, when the pore pressure increases to a threshold, the fault shows stick–slip. In the continuous slip stage, and with the continued fluid injection, the fracture stick-slips several times and this remains the predominant mode of slip.

The faults in the pressure-drive tests have already slipped in the preceding stress-drive portion of the test. The faults did not slip during the stable stage of fluid injection, indicating that the pore pressure in the fault injection borehole is higher than the pore pressure predicted by the Mohr-Coulomb failure criterion. An overpressure ratio[54] may be defined as the ratio of fluid pressure increase measured at the injection borehole at the beginning of fault instability to the pore pressure predicted by the failure criterion. It can be shown that the fluid overpressure is related to initial normal stress, shear stress and injection rate.[17,34,54] However, for a critically stressed fault, the Mohr-Coulomb failure criterion predicts a fluid pressure of 0, and the overpressure ratio of the fault cannot be calculated. Moreover, the fault overpressure ratio is strongly influenced by the fault initial stress state. Even for the same fault, different overpressure ratios might be obtained under different stress states. Therefore, we only study the effect of the overpressure on the reactivation of faults. Considering the effect of overpressure (P_{over}), the pore pressure effective stress criterion can be modified as:

$$\begin{cases} \sigma_{en} = \sigma_n \,, P_w \le P_{over} \\ \sigma_{en} = \sigma_n - \overline{P_w} - P_{over} \,, P_w > P_{over} \end{cases} \tag{15}$$

where $\overline{P_w}$ is the equivalent pore pressure in the fault.

The fluid overpressure is constant when the fluid distribution is uniform on faults and increases with a more heterogeneous fault pressure distribution as demonstrated by Passelègue et al. (2018). The fluid pressure distribution on a fault depends on the balance between fluid injection and diffusion rates.[56] A faster rate of fluid injection promotes high gradients around the injection point.[17,34,54] The rate of fluid injection can be artificially controlled. However, the heterogeneous fault pressure distribution is related to heterogeneity of the fault itself. As shown in Fig. 11, the slip zone has a high pore pressure and is reactivated during the injection. The remainder of the fault remains locked. In the initial stage of fluid injection, although the pore pressure in the injection boreholes is gradually increased, the locked area retains the fault stable.

The rate of pressure diffusion within the fault as expressed by the diffusion coefficient A, defined as:

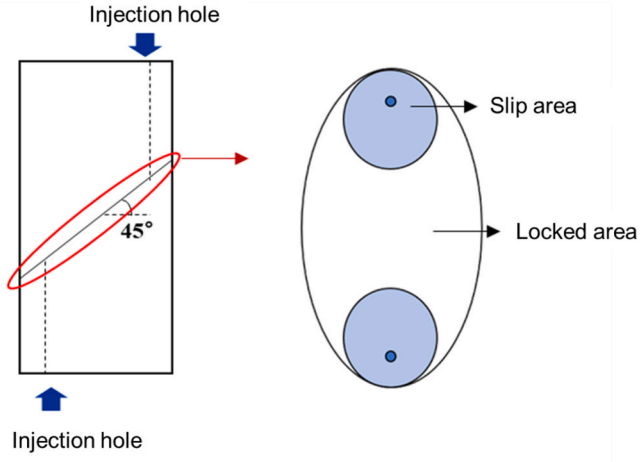

Fig. 11. Locked and slipping zones on faults. The blue area is the slip area embedded within the (white) locked area. (For interpretation of the references to colour in this figure legend, the reader is referred to the Web version of this article.)

$$A = k/\mu\alpha\Phi \tag{16}$$

where μ is fluid viscosity, α is fluid compressibility, Φ is the fault porosity and k is the fault permeability. As the fluid compressibility and dynamic viscosity, together with the fault porosity of each rock sample have the same value, the fault diffusion coefficient is a function of permeability. Therefore, the rate of pressure diffusion could also be characterized by permeability, which is an extremely important property for EGS projects. The relationship between overpressure and fault permeability, measured before fluid-pressure-driven reactivation, is shown in Fig. 12 as a negative exponential relationship between the overpressure P_{over} and fault permeability k.

The mechanism of fault slip under pressure-drive is shown in Fig. 13. During fluid injection, the shear stress produced by faults did not change in the initial stage due to the presence of overpressure, but decreased with the decreasing effective normal stress after the pore pressure exceeded the overpressure. The fault exhibited stick–slip response due to the combined mechanical and fluid loads during the increase of pore pressure, and a stress drop occurred. Subsequently, the stress path exhibits nonlinearity due to slip-strengthening and permeability evolution. During the strengthening process, the fluid pressure again increases, leading to continuous stick-slip response in the smooth faults. The evolution of friction coefficient and permeability are the main factors influencing fluid-injection-induced earthquakes and are both related to fault roughness.

4.3. Implications for injection-induced seismicity

During fluid injection, the fault is subjected to the combined effects of both stress and fluid pressure. It is important to fully understand the mechanisms of stress- and fluid-pressure-driven fault reactivation for the better assessment and control of induced earthquakes. We obtain the frictional slip characteristics of faults under stress- and fluid-pressure-driven conditions through a series of triaxial shear tests. The fault frictional slip characteristics are shown to be closely related to the roughness and permeability of the fault.

By comparing the stress- and hydraulic-driven fault slip characteristics, it is observed that under stress-driven conditions, stick–slips occurred only on the smoother faults. However, natural faults with a rougher surface showed stick–slip only at very high stress levels. For fluid injection, even the rough faults showed stick–slip response. This indicates that the risk of inducing earthquakes is extremely high once

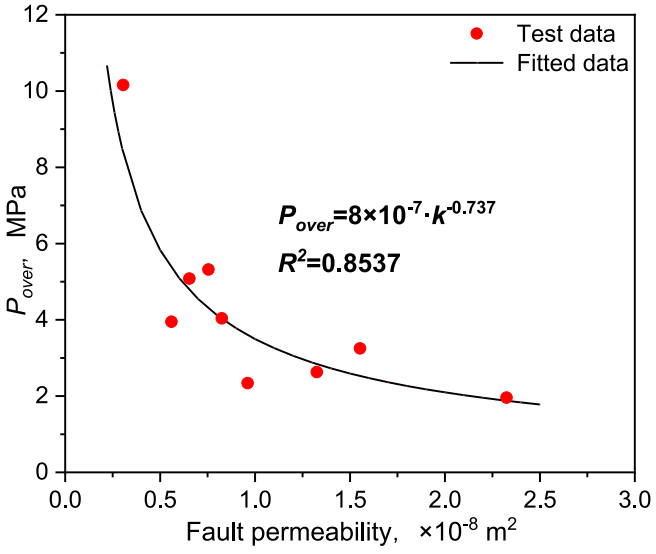

Fig. 12. Fluid overpressure and fault permeability recovered from first slip on faults that exhibited significant stick-slip.

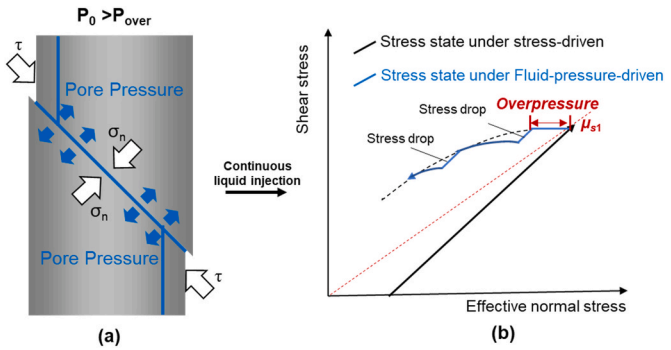

Fig. 13. Mechanism of faults reactivation under fluid-pressure-driven: (a) Schematic of fault instability; (b)Stress path of faults reactivation under fluid-pressure-driven.

the fault slips as a result of fluid injection. For example, the Duvernay hydraulic fracturing project in Western Canada[57–59] and shale gas extraction in the central and eastern United States[60,61] and EGS projects in Switzerland,[62,63] and South Korea[64,65] have all generated induced earthquakes.

At present, our determination of fault state is mainly based on the Mohr-Coulomb failure criterion and effective stress criterion. Fault slip is mainly influenced by the applied stresses and fault friction coefficient. For a fault in a critical state, the effective stress will decrease after liquid injection and the fault should slip immediately. However, the results of fluid injection induced seismicity in the central United States indicates that seismicity occurs potentially long after the injection.[66] This is potentially due to the uneven distribution of pore pressure within the fault, resulting in the fluid pressure required for fault activation often being higher than the value predicted by applying the Mohr-Coulomb failure criterion. The difference is the overpressure, making it difficult to determine the timing of injection-induced seismicity. During the injection, the pore pressure distribution in the fault is affected by various factors such as fault roughness, stress state, mineral composition, and fluid injection conditions,[20,28] resulting in a complex behavior. This experimental study shows that the overpressure required for fault reactivation is related to its permeability. Fluid injection into EGS reservoirs will elevate permeability from micro-to milli-Darcy levels. This may reduce the pore pressure required for fault reactivation and increase the risk of induced earthquakes. Therefore, during EGS fluid injection, chemical and physical means can be used to stimulate the fault to increase its roughness, thereby reducing the risk of fluid injection induced earthquakes.

Finally, it is necessary to point out that the vast majority of previous studies on fluid injection induced earthquakes, whether from laboratory or field perspectives, focused more on the instability behavior of optimal faults under regional tectonic stress state. According to the Mohr-Coulomb criterion, the angle between the optimally orientated fault and the maximum principal stress is 45°–0.5tan$^{-1}\mu$. Byerlee[29] indicated that for most rocks, the friction coefficient of the fault is ~0.6, corresponding to an optimal azimuth angle of ~30°. The 45° angle in this study is not the optimal fault orientation, regardless of the friction coefficients obtained from sawcut faults with various roughness. Due to the minimum shear stress required for the initiation of fault slip along the favorable direction, previous study results only provided the lower limit of fluid overpressure during fault slip.[56] Hence, the results of our overpressure experiment may be more universally representative. It is necessary to pay more attention to the study of fluid injection induced earthquakes in unfavorably orientated faults in the future.

5. Conclusions

To obtain the slip characteristics of faults under both stress- and

fluid-pressure-induced reactivation, we completed laboratory reactivation experiments on three groups of saw-cut faults with different roughnesses. The results show that.

(1) Under stress-driven conditions, the transition from stable slip to fault slip can be explained by the Mohr-Coulomb failure criterion. High roughness faults primarily exhibit stable slip behavior, while low roughness faults experience rapid slip accompanied by a significant stress drop. This stress relaxation leads to subsequent transition into a stable-slip state. Additionally, the rocks on the fault plane undergo strain hardening during slip, reducing their ability to deform and requiring higher stress to counteract amplified frictional forces post-slip. The friction coefficient gradually increases with multiple slip events until the strain region on the fault surface stabilizes.
(2) Under pressure-driven conditions, fault slip occurs only after the pore pressure within the fault reaches a significant overpressure. The uneven distribution of pore pressure leads to the formation of high-pressure regions near the fluid injection point, causing sliding within the fault. However, some regions within the fault remain locked, maintaining overall stability. As fluid continues to be injected, the locked regions gradually decrease until the shear stress on the fault surface exceeds the frictional resistance provided by the locked regions, resulting in fault slip.
(3) The magnitude of overpressure is influenced by permeability, with overpressure increasing as permeability decreases. During fluid injection, the shear stress produced by faults initially remains unchanged due to the presence of overpressure. However, it decreases as the effective normal stress decreases after the pore pressure exceeds the overpressure. Stick-slip response occurs due to the combined mechanical and fluid loads during the increase in pore pressure, resulting in a stress drop. The stress path exhibits nonlinearity due to slip-strengthening and permeability evolution. During the strengthening process, the fluid pressure increases again, leading to continuous stick-slip response in smooth faults. The evolution of friction coefficient and permeability are crucial factors influencing fluid-injection-induced earthquakes, and both are related to fault roughness.

These findings have significant implications for EGS projects and the mitigation of anthropogenic earthquakes in EGS. Understanding the slip characteristics of faults under different conditions can help in the design and operation of EGS projects, improving their success rate. By considering fault roughness, stress-driven and pressure-driven reactivation can be better predicted and managed, reducing the risk of induced seismicity. Additionally, the knowledge of how friction coefficient and permeability evolve during fluid injection can guide the development of strategies to minimize seismic hazards associated with EGS operations.

Declaration of competing interest

The authors declare that they have no known competing financial interests or personal relationships that could have appeared to influence the work reported in this paper.

Data availability

Data will be made available on request.

Acknowledgments

The research was funded by National Natural Science Foundation of China (Nos. 42177175, 41807222, 41941018), Central Public-interest Scientific Institution Basal Research Fund (No. DZLXJK202204), and China Geological Survey (Nos. DD20190138, DD20221660). Many thanks to Professor Zhihong Zhao from Tsinghua University for providing assistance in scanning samples and providing the program for evaluating shear damage. Bin Li helped to make granite samples. We are grateful to Dr. Yinlin Ji and an anonymous reviewer for their constructive and helpful comments and suggestions.

References

1. Lengliné O, Boubacar M, Schmittbuhl J. Seismicity related to the hydraulic stimulation of GRT1, Rittershoffen, France. *Geophys J Int. Published online January*. 2017;9:ggw490. https://doi.org/10.1093/gji/ggw490.
2. Zhang E, Wen D, Wang G, et al. The first power generation test of hot dry rock resources exploration and production demonstration project in the Gonghe Basin, Qinghai Province, China. *China Geol*. 2022;5(3):372–382. https://doi.org/10.31035/cg2022038.
3. Zhang F, Cao S, An M, Zhang C, Elsworth D. Friction and stability of granite faults in the Gonghe geothermal reservoir and implications for injection-induced seismicity. *Geothermics*. 2023;112, 102730. https://doi.org/10.1016/j.geothermics.2023.102730.
4. Zhang C, Li B, Li H, et al. Stress estimation in a 3 km-deep geothermal borehole: a snapshot of stress state in Southern Cathaysia block, China. *Tectonophysics*. 2023;864, 230031. https://doi.org/10.1016/j.tecto.2023.230031.
5. Hao M, Shen ZK, Wang Q, Cui D. Postseismic deformation mechanisms of the 1990 Mw 6.4 Gonghe, China earthquake constrained using leveling measurements. *Tectonophysics*. 2012;532–535:205–214. https://doi.org/10.1016/j.tecto.2012.02.005.
6. Jaeger JC, Cook NGW, Zimmerman R. Fundamentals of rock mechanics. *Int J Rock Mech Min Sci Geomech Abstr*. 1974;11(1):A1. https://doi.org/10.1016/0148-9062(74)92205-0.
7. Scholz C, Molnar P, Johnson T. Detailed studies of frictional sliding of granite and implications for the earthquake mechanism. *J Geophys Res*. 1972;77(32):6392–6406. https://doi.org/10.1029/JB077i032p06392.
8. Dieterich JH. Time-dependent friction and the mechanics of stick-slip. In: Byerlee JD, Wyss M, eds. *Rock Friction and Earthquake Prediction*. Birkhäuser Basel; 1978:790–806. https://doi.org/10.1007/978-3-0348-7182-2_15.
9. Palmer AC, Rice JR. The growth of slip surfaces in the progressive failure of over-consolidated clay. *Proc R Soc Lond Ser Math Phys Sci*. 1973;332(1591):527–548.
10. Dieterich JH. Modeling of rock friction: 1. Experimental results and constitutive equations. *J Geophys Res*. 1979;84(B5):2161. https://doi.org/10.1029/JB084iB05p02161.
11. Maurer J, Segall P. Magnitudes of induced earthquakes in low-stress environments. *Bull Seismol Soc Am*. 2018;108(3A):1087–1106. https://doi.org/10.1785/0120170295.
12. Galis M, Ampuero JP, Mai PM, Cappa F. Induced seismicity provides insight into why earthquake ruptures stop. *Sci Adv*. 2017;3(12), eaap7528. https://doi.org/10.1126/sciadv.aap7528.
13. van der Elst NJ, Page MT, Weiser DA, Goebel THW, Hosseini SM. Induced earthquake magnitudes are as large as (statistically) expected: induced earthquake maximum magnitudes. *J Geophys Res Solid Earth*. 2016;121(6):4575–4590. https://doi.org/10.1002/2016JB012818.
14. Feng Y, Mignan A, Sornette D, Gao K. Investigating injection pressure as a predictor to enhance real-time forecasting of fluid-induced seismicity: a bayesian model comparison. *Seismol Res Lett*. 2023;94(2A):708–719. https://doi.org/10.1785/0220220309.
15. Ji Y, Wanniarachchi WAM, Wu W. Effect of fluid pressure heterogeneity on injection-induced fracture activation. *Comput Geotech*. 2020;123, 103589. https://doi.org/10.1016/j.compgeo.2020.103589.
16. Ji Y, Fang Z, Wu W. Fluid overpressurization of rock fractures: experimental investigation and analytical modeling. *Rock Mech Rock Eng*. 2021;54(6):3039–3050. https://doi.org/10.1007/s00603-021-02453-8.
17. FrançoisX Passelègue, Brantut N, Mitchell TM. Fault reactivation by fluid injection: controls from stress state and injection rate. *Geophys Res Lett*. 2018;45(23). https://doi.org/10.1029/2018GL080470.
18. Ishibashi T, Elsworth D, Fang Y, et al. Friction-Stability-permeability evolution of a fracture in granite. *Water Resour Res*. 2018;54(12):9901–9918. https://doi.org/10.1029/2018WR022598.
19. Wang L, Kwiatek G, Rybacki E, Bonnelye A, Bohnhoff M, Dresen G. Laboratory study on fluid-induced fault slip behavior: the role of fluid pressurization rate. *Geophys Res Lett*. 2020;47(6). https://doi.org/10.1029/2019GL086627.
20. Fang Z, Wu W. Laboratory friction-permeability response of rock fractures: a review and new insights. *Geomech Geophys Geo-Energy Geo-Resour*. 2022;8(1):15. https://doi.org/10.1007/s40948-021-00316-8.
21. Zhao Q, Tisato N, Kovaleva O, Grasselli G. Direct observation of faulting by means of rotary shear tests under X-ray micro-computed tomography. *J Geophys Res Solid Earth*. 2018;123(9):7389–7403. https://doi.org/10.1029/2017JB015394.
22. Zhao Z, Peng H, Wu W, Chen YF. Characteristics of shear-induced asperity degradation of rock fractures and implications for solute retardation. *Int J Rock Mech Min Sci*. 2018;105:53–61. https://doi.org/10.1016/j.ijrmms.2018.03.012.
23. Collettini C, Di Stefano G, Carpenter B, et al. A novel and versatile apparatus for brittle rock deformation. *Int J Rock Mech Min Sci*. 2014;66:114–123. https://doi.org/10.1016/j.ijrmms.2013.12.005.
24. Ujiie K, Tsutsumi A. High-velocity frictional properties of clay-rich fault gouge in a megasplay fault zone, Nankai subduction zone: frictional property of nankai megasplay. *Geophys Res Lett*. 2010;37(24). https://doi.org/10.1029/2010GL046002. n/a-n/a.

25. Cornelio C, Spagnuolo E, Di Toro G, Nielsen S, Violay M. Mechanical behaviour of fluid-lubricated faults. *Nat Commun*. 2019;10(1):1274. https://doi.org/10.1038/s41467-019-09293-9.
26. Wu W, Reece JS, Gensterblum Y, Zoback MD. Permeability evolution of slowly slipping faults in shale reservoirs. *Geophys Res Lett*. 2017;44(22). https://doi.org/10.1002/2017GL075506, 11,368-11,375.
27. Ye Z, Ghassemi A. Injection-induced shear slip and permeability enhancement in granite fractures. *J Geophys Res Solid Earth*. 2018;123(10):9009–9032. https://doi.org/10.1029/2018JB016045.
28. Chen Y, Zhang C, Zhao Z, Zhao X. Shear behavior of artificial and natural granite fractures after heating and water-cooling treatment. *Rock Mech Rock Eng*. 2020;53(12):5429–5449. https://doi.org/10.1007/s00603-020-02221-0.
29. Byerlee JD. Frictional characteristics of granite under high confining pressure. *J Geophys Res*. 1967;72(14):3639–3648. https://doi.org/10.1029/JZ072i014p03639.
30. Brace WF, Walsh JB, Frangos WT. Permeability of granite under high pressure. *J Geophys Res*. 1968;73(6):2225–2236. https://doi.org/10.1029/JB073i006p02225.
31. Tembe S, Lockner DA, Wong TF. Effect of clay content and mineralogy on frictional sliding behavior of simulated gouges: binary and ternary mixtures of quartz, illite, and montmorillonite. *J Geophys Res*. 2010;115(B3), B03416. https://doi.org/10.1029/2009JB006383.
32. Ji Y. *Shear-Flow Characteristics of Rock Fractures and Implications for Injection-Induced Seismicity*. Nanyang Technological University; 2020. https://doi.org/10.32657/10356/143989.
33. Ji Y, Hofmann H, Rutter EH, Xiao F, Yang L. Revisiting the evaluation of hydraulic transmissivity of elliptical rock fractures in triaxial shear-flow experiments. *Rock Mech Rock Eng*. 2022;55(6):3781–3789. https://doi.org/10.1007/s00603-022-02797-9.
34. Ji Y, Wu W. Injection-driven fracture instability in granite: mechanism and implications. *Tectonophysics*. 2020;791, 228572. https://doi.org/10.1016/j.tecto.2020.228572.
35. Kakurina M, Guglielmi Y, Nussbaum C, Valley B. Slip perturbation during fault reactivation by a fluid injection. *Tectonophysics*. 2019;757:140–152. https://doi.org/10.1016/j.tecto.2019.01.017.
36. Rutter E, Hackston A. On the effective stress law for rock-on-rock frictional sliding, and fault slip triggered by means of fluid injection. *Philos Trans R Soc Math Phys Eng Sci*. 2017;375(2103), 20160001. https://doi.org/10.1098/rsta.2016.0001.
37. Cappa F, Guglielmi Y, Nussbaum C, De Barros L, Birkholzer J. Fluid migration in low-permeability faults driven by decoupling of fault slip and opening. *Nat Geosci*. 2022. https://doi.org/10.1038/s41561-022-00993-4. Published online August 11.
38. Kc B, Ghazanfari E. Geothermal reservoir stimulation through hydro-shearing: an experimental study under conditions close to enhanced geothermal systems. *Geothermics*. 2021;96, 102200. https://doi.org/10.1016/j.geothermics.2021.102200.
39. Vogler D, Amann F, Bayer P, Elsworth D. Permeability evolution in natural fractures subject to cyclic loading and gouge formation. *Rock Mech Rock Eng*. 2016;49(9):3463–3479. https://doi.org/10.1007/s00603-016-1022-0.
40. Zhao Z, Peng H, Wu W, Chen YF. Characteristics of shear-induced asperity degradation of rock fractures and implications for solute retardation. *Int J Rock Mech Min Sci*. 2018;105:53–61. https://doi.org/10.1016/j.ijrmms.2018.03.012.
41. Cappa F, Guglielmi Y, Nussbaum C, De Barros L, Birkholzer J. Fluid migration in low-permeability faults driven by decoupling of fault slip and opening. *Nat Geosci*. 2022;15(9):747–751. https://doi.org/10.1038/s41561-022-00993-4.
42. Ishibashi T, Elsworth D, Fang Y, et al. Friction-Stability-permeability evolution of a fracture in granite. *Water Resour Res*. 2018;54(12):9901–9918. https://doi.org/10.1029/2018WR022598.
43. Jia Y, Wu W, Kong XZ. Injection-induced slip heterogeneity on faults in shale reservoirs. *Int J Rock Mech Min Sci*. 2020;131, 104363. https://doi.org/10.1016/j.ijrmms.2020.104363.
44. Jeppson T, Lockner D, Taron J, et al. Effect of Thermal and Mechanical Processes on Hydraulic Transmissivity Evolution..
45. Ye Z, Ghassemi A. Injection-induced shear slip and permeability enhancement in granite fractures. *J Geophys Res Solid Earth*. 2018;123(10):9009–9032. https://doi.org/10.1029/2018JB016045.
46. Mclaskey GC, Yamashita F. Slow and fast ruptures on a laboratory fault controlled by loading characteristics: slow and fast laboratory fault ruptures. *J Geophys Res Solid Earth*. 2017;122(5):3719–3738. https://doi.org/10.1002/2016JB013681.
47. FrançoisX Passelègue, Schubnel A, Nielsen S, Bhat HS, Deldicque D, Madariaga R. Dynamic rupture processes inferred from laboratory microearthquakes: dynamic processes of stick-slip. *J Geophys Res Solid Earth*. 2016;121(6):4343–4365. https://doi.org/10.1002/2015JB012694.
48. Tsutsumi A, Shimamoto T. High-velocity frictional properties of gabbro. *Geophys Res Lett*. 1997;24(6):699–702. https://doi.org/10.1029/97GL00503.
49. Dieterich JH. Time-dependent friction and the mechanics of stick-slip. *Pure Appl Geophys PAGEOPH*. 1978;116(4-5):790–806. https://doi.org/10.1007/BF00876539.
50. Ruina A. Slip instability and state variable friction laws. *J Geophys Res Solid Earth*. 1983;88(B12):10359–10370. https://doi.org/10.1029/JB088iB12p10359.
51. Ida Y. Cohesive force across the tip of a longitudinal-shear crack and Griffith's specific surface energy. *J Geophys Res*. 1972;77(20):3796–3805. https://doi.org/10.1029/JB077i020p03796.
52. Mohammadioun B. Stress drop, slip type, earthquake magnitude, and seismic hazard. *Bull Seismol Soc Am*. 2001;91(4):694–707. https://doi.org/10.1785/0120000067.
53. Andrews DJ. Objective determination of source parameters and similarity of earthquakes of different size. In: Das S, Boatwright J, Scholz CH, eds. *Geophysical Monograph Series*. American Geophysical Union; 2013:259–267. https://doi.org/10.1029/GM037p0259.
54. Ji Y, Fang Z, Wu W. Fluid overpressurization of rock fractures: experimental investigation and analytical modeling. *Rock Mech Rock Eng*. 2021;54(6):3039–3050. https://doi.org/10.1007/s00603-021-02453-8.
55. Ji Y, Wu W, Zhao Z. Unloading-induced rock fracture activation and maximum seismic moment prediction. *Eng Geol*. 2019;262, 105352. https://doi.org/10.1016/j.enggeo.2019.105352.
56. Ji Y, Hofmann H, Duan K, Zang A. Laboratory experiments on fault behavior towards better understanding of injection-induced seismicity in geoenergy systems. *Earth Sci Rev*. 2022;226, 103916. https://doi.org/10.1016/j.earscirev.2021.103916.
57. Bao X, Eaton DW. Fault activation by hydraulic fracturing in western Canada. *Science*. 2016;354(6318):1406–1409. https://doi.org/10.1126/science.aag2583.
58. Eyre TS, Eaton DW, Zecevic M, D'Amico D, Kolos D. Microseismicity reveals fault activation before Mw 4.1 hydraulic-fracturing induced earthquake. *Geophys J Int*. 2019;218(1):534–546. https://doi.org/10.1093/gji/ggz168.
59. Eyre TS, Eaton DW, Garagash DI, et al. The role of aseismic slip in hydraulic fracturing–induced seismicity. *Sci Adv*. 2019;5(8), eaav7172. https://doi.org/10.1126/sciadv.aav7172.
60. Ellsworth WL. Injection-induced earthquakes. *Science*. 2013;341(6142), 1225942. https://doi.org/10.1126/science.1225942.
61. Keranen KM, Savage HM, Abers GA, Cochran ES. Potentially induced earthquakes in Oklahoma, USA: links between wastewater injection and the 2011 Mw 5.7 earthquake sequence. *Geology*. 2013;41(6):699–702. https://doi.org/10.1130/G34045.1.
62. Elsworth D, Spiers CJ, Niemeijer AR. Understanding induced seismicity. *Science*. 2016;354(6318):1380–1381. https://doi.org/10.1126/science.aal2584.
63. Majer EL, Baria R, Stark M, et al. Induced seismicity associated with enhanced geothermal systems. *Geothermics*. 2007;36(3):185–222. https://doi.org/10.1016/j.geothermics.2007.03.003.
64. Kim KH, Ree JH, Kim Y, Kim S, Kang SY, Seo W. Assessing whether the 2017 M_w 5.4 Pohang earthquake in South Korea was an induced event. *Science*. 2018;360(6392):1007–1009. https://doi.org/10.1126/science.aat6081.
65. Grigoli F, Cesca S, Rinaldi AP, et al. The November 2017 M_w 5.5 Pohang earthquake: a possible case of induced seismicity in South Korea. *Science*. 2018;360(6392):1003–1006. https://doi.org/10.1126/science.aat2010.
66. Keranen KM, Savage HM, Abers GA, Cochran ES. Potentially induced earthquakes in Oklahoma, USA: links between wastewater injection and the 2011 Mw 5.7 earthquake sequence. *Geology*. 2013;41(6):699–702. https://doi.org/10.1130/G34045.1.